Noncrystalline Nanocomposites as a Remedy for the Low Diffusivity of Multivalent Ions in Battery Cathodes

Yuki Orikasa, Kazuaki Kisu, Etsuro Iwama, Wako Naoi, Yusuke Yamaguchi, Yoshitomo Yamaguchi, Naohisa Okita, Koji Ohara, Toshiyuki Munesada, Masashi Hattori, Kentaro Yamamoto, Patrick Rozier, Patrice Simon, and Katsuhiko Naoi*

ABSTRACT: Rechargeable batteries using multivalent metals are among the most promising next-generation battery systems due to their high capacity, high safety, and low cost compared with lithium-ion batteries. However, strong cation−anion interaction degrades diffusion in solid cathodes, an effect that must be mitigated to yield practical multivalent metal batteries. We show that a highly defective iron phosphate−carbon composite prepared by ultracentrifugation serves as a reversible insertion/deinsertion for magnesium ions with, and operates beyond, a 2-V cell voltage at room temperature. A composite of noncrystalline particles that embeds the surrounding carbon structure enhances the magnesium-ion diffusion in the solid phase with stability for cycle life. X-ray absorption spectroscopy, transmission electron microscopy with energy-dispersive X-ray spectroscopy, and high-energy X-ray scattering measurements demonstrate magnesium-ion insertion and extraction in the defective iron phosphate without conversion reactions. This work suggests promising applications for highly defective structures as intercalation hosts for multivalent ions.

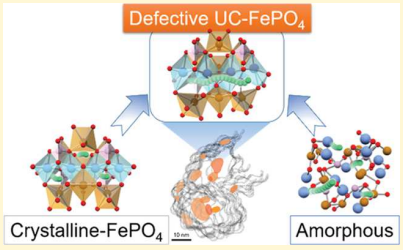

INTRODUCTION

The need for high-energy-density, abundant, inexpensive, and nontoxic metals for battery anodes has recently led to a renewal in interest from the scientific community for the use of multivalent metal anodes, such as Mg, Ca, or Al.[1] The advantages of multivalent metals include safety,[2] high energy density (e.g., increase in charge carrier density and decrease in the occupation of host structure sites by charge carrier cations), and a relatively large negative standard electrode potential,[3] although recent research on the magnesium anode has reported dendrite formation of magnesium in a specific condition.[4] Multivalent metals are also advantageous from the perspective of natural-resource conservation, a problematic aspect of lithium-ion batteries.[5]

However, despite these advantages and several years of research, applications for devices based on multivalent metals remain limited.[6,7] A key issue lies in the dramatic reduction in conductivity compared to monovalent cation systems due to strong electrostatic interactions between multivalent cations and anions. This challenge results in devices based on multivalent cations continuing to require high operating temperatures to achieve realistic operating rates, despite many years of effort (see Table S1 in the Supporting Information). The kinetics of ion insertion and deinsertion, the topochemical reactions crucial for active materials of rechargeable batteries, is particularly slow for multivalent cation systems, and designing practical devices will require novel strategies for addressing this problem.

The main challenge of multivalent cation systems is to design cathode materials as host structures for intercalation of multivalent ions that can match the performance of lithium-ion battery cathodes.[8] Although the radius of the magnesium ion (72 pm) is nearly identical to that of the lithium ion (76 pm in a hexacoordinated environment),[9] the divalent character of the magnesium ion doubles the charge density over that of the monovalent lithium ion. This reduces the solid-state (chemical) diffusivity of magnesium ion in active materials, resulting in the slow kinetics of electrochemical insertion and deinsertion. For example, Levi et al. considered the diffusion of magnesium ions in the active materials of the transition-metal-layered oxide A_xCoO_2 (A = Li, Mg)[10] and showed that when the mobile ion is located at a stable AO_6 site, the defect formation energy is larger for magnesium ions due to larger Coulomb interactions. Rong et al. performed first-principles calculations using the structure of typical lithium-ion active battery materials to estimate the diffusion barriers for lithium ions and various multivalent ions, including magnesium, zinc, calcium, and aluminum.[11] They found that the ion charge density and the anion coordination number of the insertion site within the crystal structure greatly influence the ion

https://dx.doi.org/10.1021/acs.chemmater.9b03665

diffusion barrier, which is drastically increased for a multivalent ion. Based on simple one-dimensional (1D) diffusion calculations using the diffusion length $\sqrt{Dt}$ (where D and t are the diffusion constant and the diffusion time, respectively) and the relation $D \approx a^2\nu \exp\left(\frac{-E_{act}}{kT}\right)$ between the diffusion constant and the activation energy (with a, ν, E_{act}, and kT representing the hopping length, atomic transition frequency, activation energy, and temperature in energy units, respectively), Canepa et al. showed that for activation energies >0.8 eV, particles of size ≤10 nm are required to achieve magnesium-ion insertion/deinsertion at a rate of 0.1C at room temperature (Figure S1).[8] As a result, cathode materials that usually present particle sizes >10 nm are generally operated at slow rates or elevated temperatures to improve ion diffusion for solid electrodes.

Following these theoretical advantages and disadvantages of multivalent cation batteries, we next survey previous studies of host structures used for multivalent cation insertion and extraction (see Table S1). One successful system leverages chalcogenides with Chevrel-structured Mo_6S_8[7] and spinel-structured titanium sulfide or selenide.[12,13] However, all chalcogenide-based systems studied suffer from low operating potentials and poor rate characteristics. As an alternative to chalcogenides, oxide-based host structures, such as V_2O_5 and α-MnO_2, have been considered to increase the operating potential. V_2O_5 has been used as a model system in many studies attempting to realize multivalent cation insertion/deinsertion reactions at acceptable rates, which revealed the critical role of water in the electrolytes.[14−22] Another example of a host structure is α-MnO_2, which exhibits promising properties but suffers from poor cycle performance.[23] Despite numerous advances, oxide-based cathode materials, like the chalcogenide compounds, appear incapable of meeting the performance requirements for practical multivalent cation batteries.

The difficulties encountered in constructing practical multivalent cation batteries from chalcogenides and oxides spurred researchers to consider a third family of candidate materials, polyanion compounds, which are known, from experience with lithium-ion batteries, to exhibit good performance in several key areas. For example, olivine-structured polyanion compounds exhibit high operating potential, high charge and discharge rates, and good cycle performance.[24,25] Ling et al. conducted first-principles calculations of redox potentials and lattice volumes for olivine-type compounds with and without intercalation of magnesium ions. They showed that, among the various compounds, $FePO_4$ is particularly promising because it allows magnesium-ion insertion and extraction within the electrolyte stability potential window, as well as exhibits relatively small changes in lattice volume.[26] Le Poul et al. demonstrated experimentally that up to 0.38 magnesium ions can be inserted and extracted in $FePO_4$.[27] However, these experiments were conducted at extremely slow charge/discharge rates. Subsequent work showed that, at moderate or higher rates, magnesium intercalation into $FePO_4$ fails to proceed due to instabilities in the olivine crystal structure.[28] Thus, the promising theoretical capabilities of $FePO_4$ remain unrealized in practice.

In this study, we propose and experimentally validate a strategy that uses a noncrystalline host, specifically, a $FePO_4$−carbon composite, prepared by the ultracentrifugation (UC) method we previously pioneered for fabricating electrodes for nanohybrid capacitors.[29−34] We demonstrate that UC-prepared composite electrodes allow for ultrafast insertion and deinsertion of lithium ions,[29,30] and also show that this yields high-performance electrode materials for multivalent cation rechargeable batteries. Here $FePO_4$ is selected as the electrode material due to its stable structure, reinforced by the P−O bonds, and relatively high operating potential for insertion and extraction of multivalent cations. Because the insertion and deinsertion of magnesium ions in olivine-structured $FePO_4$ crystals have been reported to be irreversible,[28] we consider the preparation of noncrystalline, highly defective $FePO_4$ to be highly dispersed throughout the carbon structure. We demonstrate that the crystallinity of the obtained active material is related to the crystallinity of the carbon used during the UC process, and triggers the efficiency and reversibility of the faradic insertion and deinsertion of multivalent cations, even at room temperature.

Furthermore, we use transmission electron microscopy, X-ray absorption spectroscopy, and the pair distribution function from X-ray total scattering to analyze the reaction mechanisms of the charge and discharge processes. Our findings show that the enhancement of multivalent cation intercalation and extraction reactions is due to (a) a reduced diffusion length with reversible ion insertion and deinsertion using nanoactive materials embedded into the carbon and (b) enhanced ionic diffusion due to the highly defective active material. We anticipate that our work will offer opportunities toward the practical realization of multivalent cation batteries.

MATERIALS AND METHODS

Synthesis of UC-Derived Materials (UC-$FePO_4$). UC-$FePO_4$ was prepared via the "ultracentrifugation (UC)" method described previously.[30] $Fe(CH_3COO)_2$, $LiCH_3COO$, and H_3PO_4 were used as the Fe, Li, and PO_4 sources, respectively, while citric acid ($C_6H_8O_7$) was used as the chelating agent. Hollow-structured Ketjen black (KB; EC600JD, Ketjen Black International) with 50- nm-diameter primary particles with a specific surface area (SSA) of 1270 $m^2\ g^{-1}$ was selected as the precursor carbon matrix for bedding the nanoscale $FePO_4$ due to its high electronic conductivity and specific surface area. Ultrapure water (17 Ω cm) was used as the medium for the entire preparation scheme.

Two solutions, A and B, were prepared. For solution A, $LiCH_3COO$, $Fe(CH_3COO)_2$, and $C_6H_8O_7$ were dissolved in H_2O and mixed at a molar ratio of 1:1:1. For solution B, H_3PO_4 solution and KB were mixed for 30 min using ultrasonication and then treated by a first UC process for 5 min to form a blackish gel. After the addition of solution A into B, a second UC treatment was performed for 5 min. Following a drying process using a spray dryer, further annealing for 8 min (3 min heating, 5 min holding) at 700 °C under a nitrogen flow yielded the UC-$FePO_4$/KB composite powder with a carbon content of 50 wt %. As discussed in Results and Discussion, the lithium source is not distributed into the $FePO_4$ particles even though it remains in the composite powder. Electrodes were prepared from the composite powder and poly(tetrafluoroethylene) (PTFE) with a weight ratio of 90:10. As a result, the weight ratio of the active material, carbon, in PTFE was 45:45:10.

Crystalline $FePO_4$. Crystalline $FePO_4$ was prepared following a two-step procedure consisting of first preparing crystalline carbon-coated $LiFePO_4$ and then further chemically oxidizing it to remove lithium. Carbon-coated $LiFePO_4$ was prepared by a solid-state reaction. Li_2CO_3, $FeC_2O_4{\cdot}2H_2O$, and $(NH_4)_2HPO_4$ were mixed at stoichiometric ratios in ethanol using a planetary ball mill with a zirconia pot and balls for 12 h at 400 rpm. After milling and drying, the precursor was mixed with 10 wt % carbon black in the ball mill for 24 h at a rotation speed of 400 rpm. The mixture was pelletized and annealed at 600 °C under a 97% argon−3% hydrogen atmosphere for

https://dx.doi.org/10.1021/acs.chemmater.9b03665

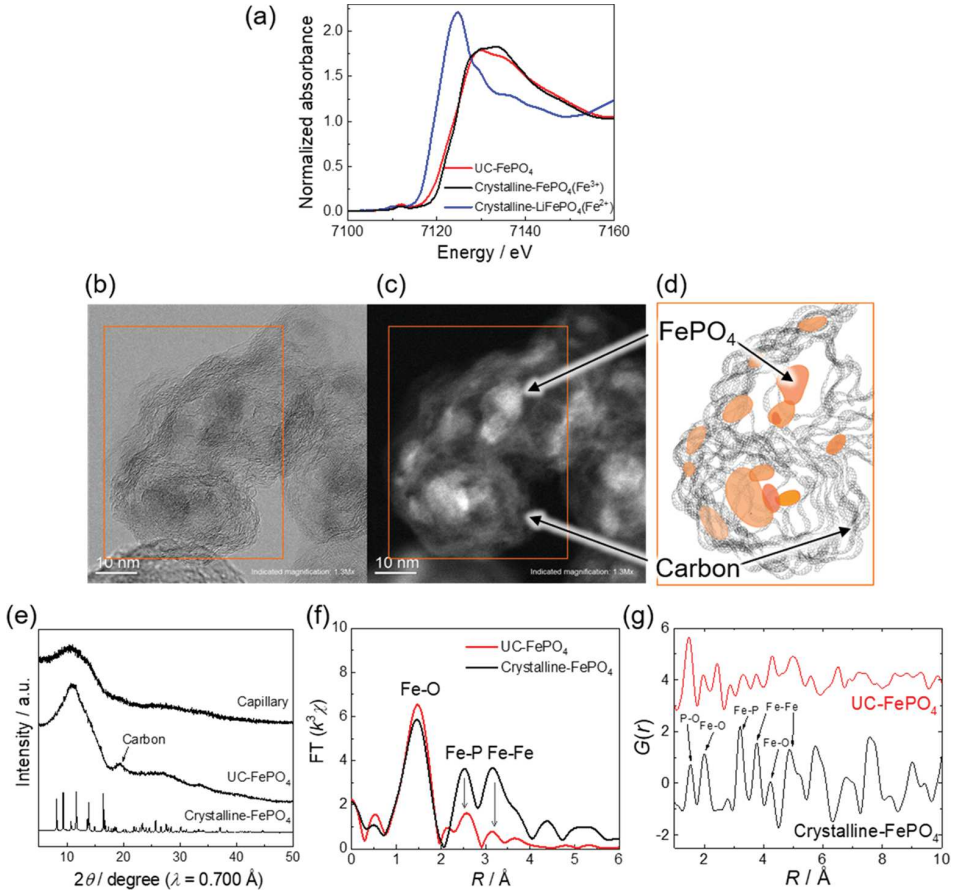

Figure 1. (a) Fe K-edge XANES spectra of the UC-$FePO_4$/KB composite, crystalline $FePO_4$ (Fe^{3+}) and crystalline $LiFePO_4$ (Fe^{2+}). (b) Bright-field and (c) dark-field TEM images of the UC-$FePO_4$ composite. (d) Schematic illustration of the UC-$FePO_4$ composite. (e) Synchrotron X-ray diffraction pattern of UC-$FePO_4$, crystalline $FePO_4$, and the glass capillary. (f) Fourier transform magnitudes from EXAFS oscillation at the Fe K-edge of UC-$FePO_4$ and crystalline $FePO_4$. (g) Reduced pair distribution functions $G(r)$ obtained from the Fourier transformation of $S(Q)$, shown in Figure S7, for crystalline $FePO_4$ and UC-$FePO_4$/KB.

6 h. $FePO_4$ was prepared by chemical oxidation from the obtained $LiFePO_4$ using nitronium tetrafluoroborate (NO_2BF_4) as an oxidizing agent. NO_2BF_4 was dissolved in acetonitrile, and then the $LiFePO_4$ powder was stirred in the solution for 48 h. The mixture was filtered and washed with acetonitrile. The results of the crystal structure analyses for the latter are shown in Figure S2 and Table S2. Electrodes were prepared from the $FePO_4$ active material, carbon black, and PTFE with a weight ratio of 45:45:10.

Electrochemical Measurements. For electrochemical lithium insertion and deinsertion, two- or three-electrode cells were prepared using metallic lithium as the reference and counter electrodes. 1 M $LiPF_6$ in a 3:7 volume ratio of ethylene carbonate (EC) and diethyl carbonate (EMC) was used as the electrolyte solution. For electrochemical magnesium insertion and deinsertion reactions, charged cells using the lithium electrolyte were dismantled in an Ar-filled glovebox. The working electrode was rinsed several times with dimethyl carbonate and dried in vacuum. Electrochemical measurements were carried out using a three-electrode cell with an Ag^+/Ag double-junction reference electrode. The counter electrode used was active carbon, and the electrolyte was 0.5 M magnesium bis(trifluoromethanesulfonyl)amide in acetonitrile [$Mg(TFSA)_2$/AN]. A titanium mesh was employed as the current collector. Galvanostatic discharge and charge measurements were performed.

X-ray Absorption Spectroscopy. For Fe K-edge X-ray absorption spectroscopy (XAS) measurements, charged and discharged electrodes were finely intermixed with boron nitride powder and pressed into pellets. These pellets were sealed in laminated packets in an Ar-filled glovebox. XAS spectra were measured near the Fe K-edge energy at room temperature in transmission mode at the beamline of the SPring-8 synchrotron radiation facility (BL01B1 and BL14B2) in Hyogo, Japan, and data were collected at room temperature. Extended X-ray absorption fine structure (EXAFS) analysis was performed using REX2000 data analysis software with the theoretical backscattering phases and amplitudes calculated using the FEFF8 code.

X-ray Total Scattering Measurement. The high-energy X-ray total scattering measurement was conducted at room temperature at the SPring-8 high-energy X-ray diffraction (XRD) beamline BL04B2 using a two-axis diffractometer. The incident X-ray energy obtained from a Si(220) crystal monochromator was 61.4 keV. The diffraction patterns of the samples were measured at angles from 0.3 to 48°. The intensity of the incident X-ray was monitored in an ionization chamber filled with Ar gas, and the scattered X-rays were observed by CdTe detectors. The collected datasets were corrected for absorption, background, and polarization effects.

Transmission Electron Microscopy. The UC-$FePO_4$ composite nanostructure and particle size distribution were characterized using high-resolution transmission electron microscopy (TEM) (Hitachi models H9500 and HD2700). Only the UC-$FePO_4$ composite and KB were subjected to electrical measurements using the nanoprobing system Hitachi N-6000SS.

https://dx.doi.org/10.1021/acs.chemmater.9b03665

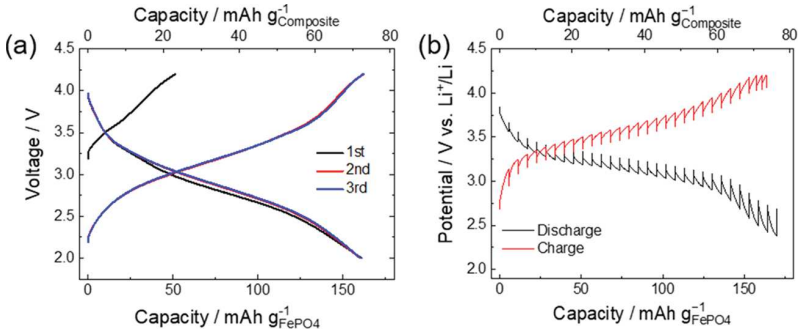

Figure 2. (a) Charge/discharge profile of UC-$FePO_4$/KB at 1C rate with 1 M $LiPF_6$/EC-EMC. (b) Galvanostatic intermittent titration technique profile of UC-$FePO_4$/KB with 1 M $LiPF_6$/EC-EMC.

RESULTS AND DISCUSSION

Characterization of a Pristine UC-Prepared $FePO_4$−Carbon Composite Material. *Composition and Morphology Analysis.* Fe K-edge X-ray absorption near-edge structure (XANES) analysis of the as-prepared $FePO_4$−Kejenblack composite (pristine UC-$FePO_4$/KB) by the ultracentrifugation method (Figure 1a) exhibits an absorption edge energy nearly identical to that of crystalline $FePO_4$, which shows that iron has solely the trivalent state, in agreement with the chemical formulae of $FePO_4$. However, inductively coupled plasma (ICP) analysis of the sample shows that Fe and P, as well as Li, are present in equal quantities (atomic composition ratio Li/Fe/P = 1.0:1.0:1.0). Together with the XANES results, this observation supports the presence of lithium in the graphitic KB carbon phase, not in FP. The composite corresponds then to a mixture of pure $FePO_4$ and Li-doped KB.

Figure 1b,c shows bright- and dark-field TEM images of the pristine UC-$FePO_4$/KB, and observations at several magnifications are shown in Figure S3. The images show particles with sizes around 10 nm embedded in KB (random graphitic carbon), as designated by the schematic representation in Figure 1d, which confirms the benefit of the UC treatment for preventing grain growth and agglomeration. In addition, the strong interaction between the $FePO_4$ particles and carbon is confirmed by the comparison of the conductivity measured for the pristine UC-$FePO_4$/KB, which is higher than that of KB alone (Figure S4).

Crystal Structure Analysis. The XRD pattern seen in Figure 1e exhibits broad peaks at 10° and near 18°, attributed to the glass capillaries and the carbon, respectively, with no evidence of $FePO_4$ Bragg peaks. Also, a clear lattice image cannot be confirmed by the TEM observation of our UC-$FePO_4$/KB composite. On the other hand, the existence of short- and medium-range ordering is demonstrated by the radial distribution functions obtained from the EXAFS measurements (see Figures 1f and S5), which indicate atomic correlations persisting to large distances associated with second- and third-nearest-neighbor atoms. This coexistence of short- and medium-range orders with long-range disorder demonstrates that the state of the pristine UC-$FePO_4$/KB is not fully amorphous but highly defective. This feature also demonstrates that pristine UC-$FePO_4$/KB prepared using random graphitic carbon, the KB, includes a highly defective structure without long-range order. To confirm the importance of the crystallinity of the carbon matrix used as a UC precursor, we synthesized another composite using well-crystallized and multiwalled carbon nanotubes as the carbon matrix. XRD and TEM characterization techniques (Figure S6) unambiguously show the formation of the well-crystallized (long-range-ordered) $LiFePO_4$ with an epitaxial olivine crystal growth along the crystal face of the carbon nanotube, indicating that the lithium source is maintained in the $LiFePO_4$ particles, and a very strong interaction exists with the carbon in which they are embedded.

In contrast, with samples prepared with KB, carbon regions are highly disordered following the UC treatment, preventing the emergence of long-range ordering during crystal growth. The nature of carbon impacts (1) the location of Li that changes the valence state of Fe and (2) the crystallinity of the active material sample. The former effect has not been analyzed, and further investigations are required. In our previous study, the core−shell nanocomposite composed of crystalline $LiFePO_4$ and the highly defective amorphous phase containing Fe^{3+} encapsulated by a graphitic carbon was prepared using the UC process.[30] While this study used the slow drying process with a vacuum oven, our current synthesis utilized the spray drying method. This rapid drying process could prevent the particle growth of the thermodynamically stable $LiFePO_4$ crystal.

Figure 1g shows the pair distribution functions (PDFs) of the crystalline $FePO_4$ and the UC-$FePO_4$/KB. The total structure factors, $S(Q)$, are provided in Figure S7. The experimental PDF profile of the crystalline $FePO_4$ agrees well with the simulation profile based on the crystal structure of the crystalline $FePO_4$ (Figure S8a). The first peak at 1.5 Å is related to the P−O correlation associated with PO_4 polyanions, and the second and third peaks at 2.1 and 2.4 Å correspond to the Fe−O correlation in FeO_6 octahedra and the O−O correlation in PO_4 tetrahedra, respectively. Both peaks at 2.8 and 3.2 Å are related to the Fe−P correlation, which may overlap with the O−O correlations in the FeO_6 octahedra, while all peaks observed above 3.5 Å involve various types of bonds that cannot be easily deconvoluted.

For the UC-$FePO_4$/KB, the correlations are visible up to only 5 Å, which is in perfect agreement with the loss of the long-range ordering previously observed using XRD. Characteristic points in the profile of UC-$FePO_4$/KB include the high-intensity peak located at 1.4 Å and a new peak observed at 2.4 Å, which can be attributed to the contribution of the C−C bonds derived from KB (where the first- and second-neighbor C−C bonds in the layer structure of graphite are 1.42 and 2.46 Å).[35] Comparing the trivalent crystalline $FePO_4$ with UC-$FePO_4$/KB, the shift toward lower values of the peak located at 2 Å shows a lowering of the Fe−O interatomic distance,

https://dx.doi.org/10.1021/acs.chemmater.9b03665

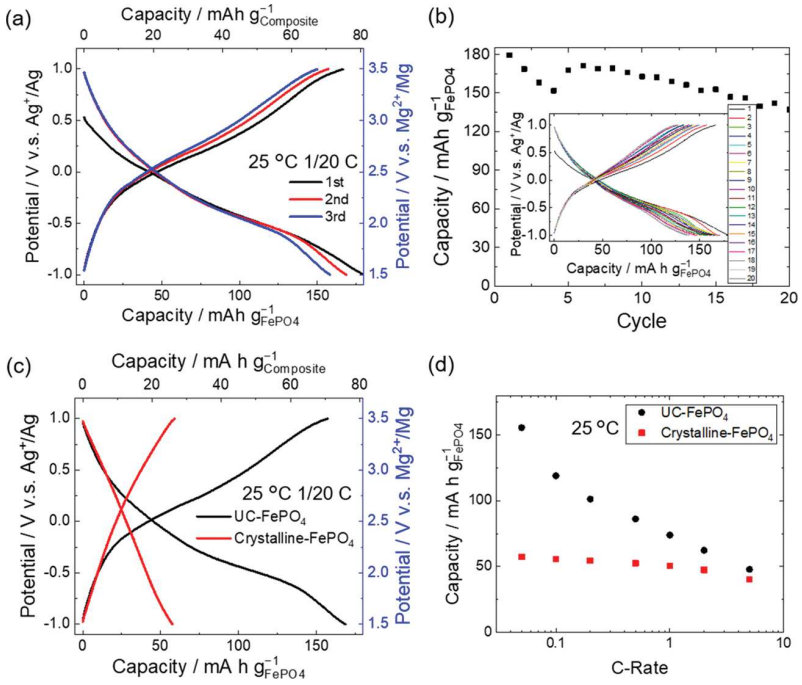

Figure 3. (a) Charge/discharge profile of the treated UC-$FePO_4$/KB composite electrode at 1/20C rate and 25 °C with 0.5 M $Mg(TFSA)_2$/AN. (b) Discharge capacity from the cycle test of the treated UC-$FePO_4$/KB composite electrode at 1/20C rate and 25 °C with 0.5 M $Mg(TFSA)_2$/AN. (c) Comparison of the charge/discharge property for a Mg rechargeable battery cathode between UC-$FePO_4$/KB and crystalline $FePO_4$. (d) Rate capability of UC-$FePO_4$/KB and crystalline $FePO_4$ in the discharge mode in 0.5 M $Mg(TFSA)_2$/AN at 25 °C.

indicating the contraction of FeO_6 octahedra in UC-$FePO_4$/KB. Meanwhile, the comparison of the correlations above 3 Å, which are characteristic of medium-range ordering, shows an increase of all the interatomic distances of UC-$FePO_4$/KB, implying a larger free volume in UC-$FePO_4$/KB than in crystalline $FePO_4$.

Electrochemical Behavior. We first use Li half-cells to compare the electrochemical behavior of pristine UC-$FePO_4$/KB and crystalline $FePO_4$ samples. Figure 2a shows the charge/discharge curves for the pristine UC-$FePO_4$/KB using a lithium-ion battery electrolyte. As discussed above, the Fe K-edge XANES results confirm that Fe in pristine UC-$FePO_4$/KB exists nearly exclusively at the valence state of +3, and, thus, the Fe^{3+}/Fe^{2+} redox couple makes almost no contribution to the initial charge cycle, at which point the cell might be expected to exhibit near-zero capacity on first charging. As a result, the capacity of about 50 mAh g^{-1} measured during the first charge (the black curve in Figure 2a) is due to nonfaradic reactions involving KB. During subsequent discharging and charging reactions, the Fe^{3+}/Fe^{2+} redox couple is active and delivers a capacity of 110 mAh g^{-1}, yielding, taking into account the extra capacity due to Li−KB reaction, a total capacity of 160 mAh g^{-1}.

As noted above, the results of the XANES measurements demonstrate that lithium, although present in equal abundance with iron, is only present in the KB part of the composite and should have no effect on the overall electrochemical behavior of $FePO_4$. To confirm that, an extra UC-$FePO_4$/KB composite synthesized following the chemical process described above but without the lithium reactant has been prepared. The electrochemical tests show that this Li-free composite, besides exhibiting the same nonfaradic capacity at the first charge, delivers a lower charge/discharge capacity compared to samples prepared with the lithium reactant (Figure S9). This result shows that lithium, despite not contributing to the charge/discharge capacity, plays an indirect role. This, though currently under investigation, can be speculated to be related to the enhancement of the composite's conductivity, allowing reaching a capacity close to the theoretical one of $FePO_4$.

To investigate the structural evolution of our synthesized materials in response to the lithium intercalation during cycling, we conduct intermittent charge and discharge tests on the pristine UC-$FePO_4$/KB electrodes using a three-electrode cell setup. The resulting curves from the open-circuit potential vs charge/discharge state are plotted in Figure 2b and show a slopping potential profile different from the well-known broad plateaus typically obtained for crystalline $FePO_4$ (Figure S10). While the plateaus are a typical indicator of a two-phase coexistence, the continuous potential variation observed for UC-$FePO_4$/KB corresponds to a continuous variation of the lithium chemical potential through the electrode, indicating the absence of phase separation. Therefore, the pristine UC-$FePO_4$/KB remains in a single phase throughout the process of the lithium-ion insertion and deinsertion. This finding agrees with previously reported results for amorphous $FePO_4$.[36−39] The formation of Fe_2O_3/Li_3PO_4 nanocomposite can be ruled out as the voltage range used in this experiment excludes the possibility of activating the corresponding redox couple with a voltage reported to be <2.0 V.[40]

Charge/Discharge Properties of Pristine UC-$FePO_4$ as a Cathode Material for Magnesium-Rechargeable Batteries. The electrochemical magnesium-ion insertion and deinsertion in the UC−composite were investigated next. Although lithium's contribution to the electrochemical reaction is not significant (see the XANES experiments), pristine UC-$FePO_4$/KB samples were first electrochemically

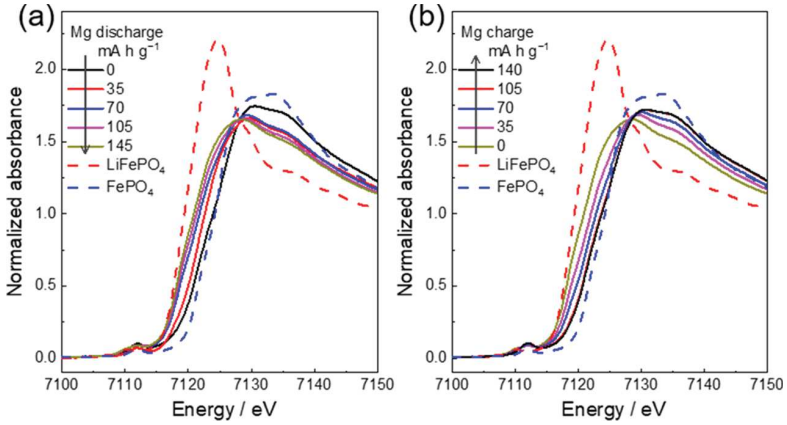

Figure 4. Normalized Fe K-edge XANES spectra of a UC-$FePO_4$/KB electrode (a) during Mg discharge and (b) during Mg-charge processes at 55 °C with 0.5 M $Mg(TFSA)_2$/AN. The dashed lines represent the standard sample data.

oxidized (delithiated) before running the experiments in the Mg-containing electrolytes. The electrochemical extraction of lithium was achieved in a Li-containing electrolyte solution. Then, the fully oxidized sample was rinsed several times with a dimethyl carbonate solvent and dried in vacuum. These samples, noted as "treated UC-$FePO_4$/KB", were then characterized in a three-electrode cell using Ag^+/Ag as a reference electrode and 0.5 M magnesium bis-(trifluoromethanesulfonyl)amide in an acetonitrile electrolyte. We also conducted the charge/discharge measurement in the Mg-containing electrolyte using the pristine UC-$FePO_4$/KB samples (Figure S11).

Figure 3a shows the charge/discharge profiles of the treated UC-$FePO_4$/KB in the magnesium electrolyte beginning in the discharge mode and operating at room temperature at a C/20 rate. All experiments were achieved in anhydrous conditions (electrolyte water content <300 ppm), so the water-assisted cointercalation reactions reported previously for V_2O_5 cannot be observed.[19] A reversible capacity of 150 mAh g^{-1} at an average potential of 2 V vs Mg^{2+}/Mg, converted according to the literature,[41] was observed and remained stable over several cycles (Figure 3b). The discharged sample was analyzed ex situ by electron energy loss spectroscopy (EELS). From the measured spectrum shown in Figure S12, an atomic weight ratio for Fe/Mg of 75:25, corresponding to a composition $Mg_{0.33}FePO_4$, was found for the particles.

The results demonstrate that, in contrast to the conventional belief that the use of magnesium requires high temperatures and very low cycling rates,[12,23,42−44] the samples prepared using the UC treatment and the control it offers over the morphology and the crystalline state of $FePO_4$ exhibit significant activation of the reversible insertion of Mg^{2+} ions even at room temperature and moderate cycling rates.

Figure 3c compares the second-cycle charge/discharge behavior of the crystalline $FePO_4$ active material to that of the treated UC-$FePO_4$/KB. To ensure we assessed the charge/discharge properties of the two materials under comparable conditions, we used a modified synthesis procedure for the crystalline $FePO_4$ electrodes to raise their carbon content to 45 wt %, equal to that of the treated UC-$FePO_4$/KB electrodes, although these carbon structures between the two electrodes are not similar to each other. Whereas crystalline $FePO_4$ exhibits low capacity at room temperature, the treated UC-$FePO_4$/KB exhibits a significantly improved charge/discharge capacity of about 150 mAh g^{-1}. This observation demonstrates that the use of highly defective UC-$FePO_4$/KB, whose crystal structure differs significantly from that of crystalline materials, enables reversible magnesium-ion insertion and deinsertion in cathode materials. Figure 3d compares the rate capabilities of these two materials. For crystalline $FePO_4$, the capacity is low and remains constant through cycling at rates ranging from C/20 to 10C, corresponding to the contribution of nonfaradic reactions due to the added carbon content. In contrast, the observed capacity for the treated UC-$FePO_4$/KB composite depends strongly on the C rate, which decreases drastically from 150 mAh g^{-1} at C/20 to 50 mAh g^{-1} at 10C. This result indicates the occurrence of faradic reactions that correspond to the insertion of magnesium ion into $FePO_4$ along with the nonfaradic reaction due to carbon.

The capacity measured at a high rate (50 mAh g^{-1}) is assumed to correspond to the nonfaradic surface contribution of the carbon from the composite, which should remain constant at any cycling rate. For reference, the charge−discharge tests using only KB with no active materials exhibited a capacity of approximately 50 mAh g^{-1} of KB (Figure S13), which is in good agreement with the capacity observed for UC-$FePO_4$/KB at high rates. As a result, at the low C/20 rate, a capacity of 100 mAh g^{-1} for the magnesium insertion can be estimated and compared to the capacity of 177 mAh g^{-1} calculated for the full reduction of Fe^{3+} down to Fe^{2+} ($Mg_{0.5}FePO_4$). Assuming the faradic reaction corresponds only to the insertion process of the magnesium ion into $FePO_4$, the composition after discharge corresponds to $Mg_{0.28}FePO_4$.

However, because of the phase separation between the transition-metal oxide and MgO being reported to be more thermodynamically stable than that for the magnesium-inserted crystal structure,[45] the possibility of such a phase separation in the case of a polyanionic compound should be considered. Zhang et al. reported, based on thermodynamic calculations, that under reducing condition[28] $Mg_{0.5}FePO_4$ should be decomposed following

$$6\ Mg_{0.5}FePO_4 \rightarrow Mg_3(PO_4)_2 + 2\ Fe_3(PO_4)_2$$

and for the oxidizing condition $Fe_3(PO_4)_2$ will form Fe_2O_3, $FePO_4$, and $Fe_7(PO_4)_6$. The kinetic effects, well known to prevent the formation of thermodynamically stable phases, are not considered here.

https://dx.doi.org/10.1021/acs.chemmater.9b03665

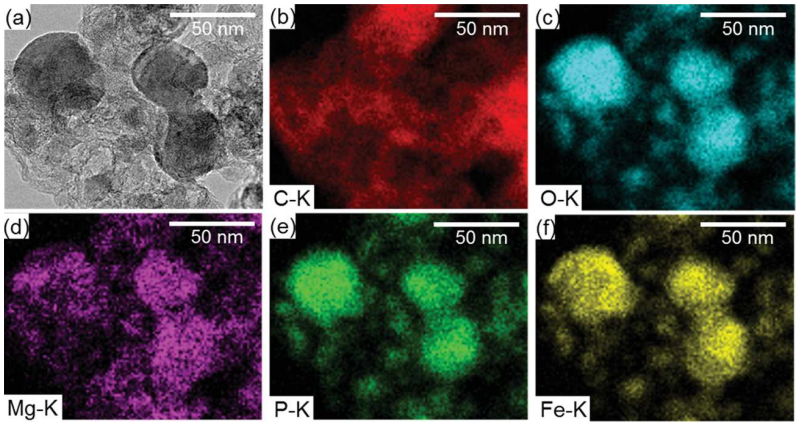

Figure 5. (a–f) Results from the TEM-EDS observation of the UC-$FePO_4$/KB composite after the first discharge using 0.5 M $Mg(TFSA)_2$/AN.

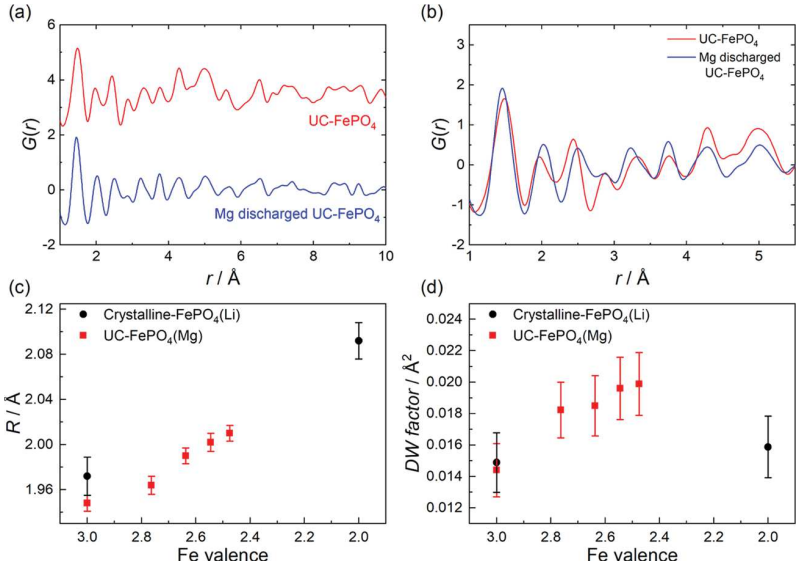

Figure 6. (a) Reduced pair distribution functions $G(r)$ obtained from the Fourier transformation of $S(Q)$ for UC-$FePO_4$/KB and discharged UC-$FePO_4$/KB in Mg electrolyte and (b) the enlarged figure. Fitting results of EXAFS analysis of UC-$FePO_4$/KB and crystalline $FePO_4$: (c) Fe–O interatomic distance and (d) Debye–Waller factor as a function of Fe mean valence calculated from the XANES two-component analysis.

To investigate if the phases resulting from such a thermodynamically driven separation are formed, a XANES analysis was performed ex situ on samples electrochemically charged and discharged at 55 °C to minimize the kinetic effects and reach thermodynamically stable states. Fe K-edge XANES spectra of charged and discharged UC-$FePO_4$/KB with the magnesium electrolyte were compared with those of different iron-based compounds used as standards (Figure S14). The XANES of Fe_2O_3 and FeO exhibit the characteristic peaks at 7131 and 7142 eV, respectively, which are not observed in the charged and discharged UC-$FePO_4$/KB. This XANES result rules out the formation of iron oxide, but cannot confirm the absence of $Fe_3(PO_4)_2$ due to similar Fe^{2+} oxygenated surroundings (as in the XANES spectra) with discharged Mg_xFePO_4. In Figure 4a, the absorption edge at the Fe K-edge shifts downward in energy, reflecting the reduction of iron ions to maintain electrical neutrality upon the magnesium-ion insertion in the discharge reaction. This shift being observable at the early stage of the discharge process suggests that the reduction of Fe^{3+} to Fe^{2+} occurs before the nonfaradic process at the end of discharge.

XANES measurements are achieved for the various charged and discharged states to obtain further insights into the reaction mechanism. During discharge (intercalation), the Fe XANES signals shift to lower energy, evidencing a decrease in the oxidation state of Fe without reaching the value characteristic of a full iron reduction, as observed in $LiFePO_4$. Moreover, the shape of the XANES curve near the intensity peak at 7124 eV is quite different from that of $LiFePO_4$, which confirms again that some iron ions remain at the (+III) valence state. During charge (Figure 4b), the oxidation of Fe ions proceeds and the XANES curve overlaps with that of the treated UC-$FePO_4$/KB, showing that the change in the valence of iron ions due to the insertion and deinsertion of magnesium ions is reversible. In a two-phase coexistence reaction between $LiFePO_4$ and $FePO_4$, Fe K-edge XANES provides isosbestic points,[46] which cannot be observed, considering the enlarged view around 7128 eV (Figure S15). Although this indeterminate crystal structure precludes the definition of

precise phases, these results confirm that the insertion and deinsertion of magnesium ions in UC-$FePO_4$ are not two-phase reactions. The deconvolution of the XANES spectra in terms of Fe^{2+} and Fe^{3+} contributions was performed (Figure S16) to estimate the composition of the fully discharged sample. A composition of $Mg_{0.22}FePO_4$ was found, which is close to the rough estimation that corresponds with the discharge faradic capacity responsible for Mg intercalation and EELS analysis.

To further investigate the possibility of the existence of a phase separation mechanism between $Fe_3(PO_4)_2$ and $Mg_3(PO_4)_2$, we performed TEM-EDS measurements. As seen in the transmission image of the electrodes after discharge (Figure 5a), the structure of the $FePO_4$ particles embedded in carbon is preserved. The element mapping images (Figure 5b–f) show that Fe, P, and O are located in the same region that does not overlap with regions in which C is observed, confirming that the composite is made of $FePO_4$ particles embedded in carbon. In addition, the intensity of Mg is observed only in regions where $FePO_4$ particles exist, which confirms that no phase segregation of $Fe_3(PO_4)_2$ and $Mg_3(PO_4)_2$ occurs.

The low-crystalline nature of UC-$FePO_4$/KB complicates XRD analysis, so we used the total X-ray scattering and EXAFS analysis to evaluate the local structural changes. Figure 6a,b shows the reduced pair distribution functions (PDF) of the treated UC-$FePO_4$/KB (before Mg discharge) and the discharged UC-$FePO_4$/KB (after Mg discharge). The PDF profile of UC-$FePO_4$/KB and the discharged sample appear quite similar with primilary peak shifts observed. The most apparent shift corresponds to the one toward higher values of the peak located close to 2 Å, attributed to Fe–O interatomic distances, which is in perfect agreement with the reduction of the Fe valence state and related increase of the Fe ion radius. Two other shifts are observed during Mg insertion toward higher and lower values for the peaks located at 2.5 and 3.2 Å, respectively. Without any structure data for the discharged sample, and knowing the similarity in the crystalline chemistry of Mg and Li, we simulated the PDF profile for a virtual $Mg_{0.5}FePO_4$ that was considered isostructural with $LiFePO_4$ and compared it with those calculated for crystalline $FePO_4$ and $LiFePO_4$ (Figure S8). Based on this comparison, we consider that, besides the reduction of iron ions, the insertion of Mg in the $FePO_4$ structure induces the appearance of a peak close to 2.5 Å attributed to Mg–P interatomic distances and another close to 3.2 Å corresponding to the overlap of several contributions, including those from Mg–Mg correlations. Despite being based on a hypothetical structure, this information allows explanation of the evolution of the PDF profiles during Mg insertion. These shifts of the peaks located around 2.5 and 3.2 Å can effectively be interpreted as a result of the overlap of the peaks already present in the treated UC-$FePO_4$/KB (with a C–C interatomic distance of 2.4 Å and Fe–P interatomic distance of 3.4 Å) with the Mg-based interatomic distances. Although the structural analysis of UC-$FePO_4$/KB is complicated, and an accurate simulation cannot be achieved, this experimental PDF result captures the magnesium-ion insertion behavior.

The evolution of the local surrounding during Mg insertion and deinsertion also follows using EXAFS analysis, which provides a probe of the local distortion simulated by the use of the Debye–Waller factor (Figures S17 and S18) in addition to the interatomic distances. The evolution of the Fe–O interatomic distance and degree of distortion of the FeO_6 octahedra versus the depth of discharge estimated from the calculation of the average Fe valence state are represented in Figure 6c,d, respectively. They confirm that the Fe–O interatomic distance increases linearly during the discharge process, which agrees with a solid solution mechanism. In addition, the slope of the evolution of the interatomic Fe–O distance as a function of the Fe valence state in UC-$FePO_4$ is nearly similar to the one calculated considering the $LiFePO_4$ and $FePO_4$ crystal structures, which indicates that the local structure change of the neighbor FeO_6 shell is influenced solely by the ionic radii of the iron ion. These two results are in good agreement with the observed PDF analysis in Figure 6a. The provided PDF and EXAFS data also exclude the formation of Fe domain and confirm the absence of conversion reaction.

We have provided four evidences of the electrochemical magnesium insertion/deinsertion of UC-$FePO_4$/KB: (1) existence of Mg species in $FePO_4$ matrix by TEM–EELS (Figure S12), (2) faradic reaction of iron ion in UC-$FePO_4$ by Fe K-edge XANES (Figure 4), (3) excluding of phase separation during charge/discharge in magnesium electrolytes by EDS (Figure 5), and (4) correlation between magnesium and $FePO_4$ matrix by X-ray PDF analysis (Figure 6). Therefore, the primary reaction discussed in this study is focused on electrochemical magnesium insertion/deinsertion in the $FePO_4$ matrix.

DISCUSSION

Conventional approaches to the design of optimal intercalation hosts typically focus on the crystal structures of the materials. For example, $LiCoO_2$, $LiMn_2O_4$, and $LiFePO_4$, which are lithium-ion battery cathode materials,[25,47,48] have stable lithium-ion sites and stable host structures accompanying reversible insertion and extraction for a wide range of lithium. The insertion and deinsertion of magnesium ions in these types of structures are associated with large activation energy for Mg^{2+} hopping between adjacent sites,[11] which hinders the development of suitable cathode materials. For example, in the olivine crystal structure, motion between magnesium sites must proceed through an extremely narrow bottleneck, which is the main factor slowing diffusion in this rigid crystal structure (Figure 7).[11] In contrast, an amorphous structure, such as V_2O_5–P_2O_5 glasses, has a diffusion barrier that is partly relieved but the cycle performance is not reversible.[49] With

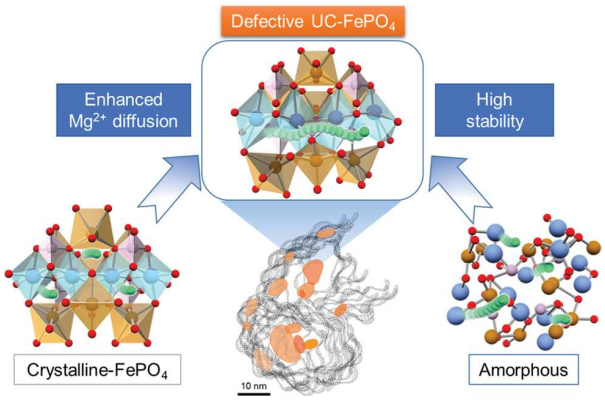

Figure 7. Reaction model for Mg diffusion in the UC-$FePO_4$ composite electrode.

https://dx.doi.org/10.1021/acs.chemmater.9b03665

UC-$FePO_4$/KB, as prepared in this study and unlike the other extreme cases, the XRD and scattering experiments show that while the long-range ordering is suppressed the short-range ordering (i.e., in the local structure of Fe−O−P) is preserved, and middle-range ordering (i.e., the connection between the different oxygenated polyhedra) is weakened, as observed through the broadening of the high correlation at high r values. This result evidences some flexibility of the structure, which then accommodates free spaces such as the free volume observed in glass. Therefore, smooth diffusion pathways through the solid are created, allowing even strongly interacting divalent magnesium ions to move through the solid phase. Our previous report demonstrated that the redox reaction in noncrystalline components exhibits no diffusion limitation within a large potential scan rate range.[50] Here, the UC process results in nano-$FePO_4$ particles with a noncrystalline structure embedded in graphitic carbon, which provides an efficient environment for reversible electrochemical insertion and deinsertion of magnesium ions. However, as shown in Figure 3a, the large hysteresis is still observed for magnesium charge−discharge, where the potential change at the beginning of the charging (magnesium deinsertion process) is obvious. This confirms the strong interaction between Mg^{2+} and the anion, which, while facilitating the insertion process, prevents easy extraction of stabilized Mg ions.

The particle size of the noncrystalline (middle-range-ordered) $FePO_4$ is particularly small (10 nm) compared to the one used for the battery application. The experimental control of particle size while maintaining the noncrystallinity of $FePO_4$ may further provide crucial evidence showing the advantage of using defective structured active material. However, small particle size and noncrystallinity of $FePO_4$ are inseparable factors, as metastable noncrystalline $FePO_4$ particles can be stabilized only within the carbon framework of KB. In our previous study, we demonstrated that the nanoparticles are required to be encapsulated within the KB to maintain noncrystallinity. Naturally, the $FePO_4$ particles embedded/encapsulated in KB become smaller than the inner space of KB (few 10 nm).

CONCLUSIONS

We demonstrated that a hybridized structure of nano-UC-$FePO_4$/KB particles embedded in carbon could operate as a host structure for multivalent cation insertion and extraction at moderate rate conditions at room temperature. Magnesium ions were reversibly inserted into UC-$FePO_4$, leading to a capacity of 160 mAh g^{-1} with an operating voltage of 2 V vs Mg^{2+}/Mg, which makes our UC-$FePO_4$/KB composite interesting as the cathode for a magnesium-ion rechargeable battery cathode. Fast reversible ion intercalation reactions were favored by the medium- and long-range structural disorders, as well as the unique morphology resulting from carbon embedding, achieved during the UC synthesis process. These findings, showing that the charge and discharge reaction characteristics of magnesium ions are improved by the careful control of the crystallinity and the structure, offer significant utility for future material designs and represent an important advance toward the realization of multivalent-ion batteries.

ASSOCIATED CONTENT

Supporting Information

The Supporting Information is available free of charge at https://pubs.acs.org/doi/10.1021/acs.chemmater.9b03665.

Representative multivalent-ion battery cathodes, additional XRD, SEM, TEM, XANES, EXAFS, PDF, nanoprobe, and electrochemical data; relationship between the diffusion length in active materials and the activation energy under various rates and temperature conditions; and refined crystal parameters and reliability factors (PDF)

AUTHOR INFORMATION

Corresponding Author

Katsuhiko Naoi − *Department of Applied Chemistry, Tokyo University of Agriculture & Technology, Koganei 184-8588, Japan;* orcid.org/0000-0002-0265-2235; Email: k-naoi@cc.tuat.ac.jp

Authors

Yuki Orikasa − *Department of Applied Chemistry, Ritsumeikan University, Kusatsu 525-8577, Japan;* orcid.org/0000-0002-9869-9520

Kazuaki Kisu − *Department of Applied Chemistry, Tokyo University of Agriculture & Technology, Koganei 184-8588, Japan*

Etsuro Iwama − *Department of Applied Chemistry, Tokyo University of Agriculture & Technology, Koganei 184-8588, Japan*

Wako Naoi − *Division of Arts and Sciences, K & W Inc., Kunitachi 186-0002, Japan*

Yusuke Yamaguchi − *Department of Applied Chemistry, Ritsumeikan University, Kusatsu 525-8577, Japan*

Yoshitomo Yamaguchi − *Department of Applied Chemistry, Ritsumeikan University, Kusatsu 525-8577, Japan*

Naohisa Okita − *Department of Applied Chemistry, Tokyo University of Agriculture & Technology, Koganei 184-8588, Japan*

Koji Ohara − *The Research & Utilization Division, Japan Synchrotron Radiation Research Institute (JASRI), Hyogo 679-5198, Japan;* orcid.org/0000-0002-3134-512X

Toshiyuki Munesada − *Graduate School of Human and Environment Studies, Kyoto University, Kyoto 606-8501, Japan*

Masashi Hattori − *Graduate School of Human and Environment Studies, Kyoto University, Kyoto 606-8501, Japan*

Kentaro Yamamoto − *Graduate School of Human and Environment Studies, Kyoto University, Kyoto 606-8501, Japan;* orcid.org/0000-0002-8739-4246

Patrick Rozier − *CIRIMAT, Université de Toulouse, CNRS, Université Toulouse 3 − Paul Sabatier, 31062 Toulouse Cedex 9, France*

Patrice Simon − *CIRIMAT, Université de Toulouse, CNRS, Université Toulouse 3 − Paul Sabatier, 31062 Toulouse Cedex 9, France;* orcid.org/0000-0002-0461-8268

Author Contributions

Y.O. conceived and designed the project and analyzed the experimental data. K.K., E.I., and N.O. prepared highly dispersed defective $FePO_4$. W.N. measured the transmission electron microscopy. T.M., Yu.Y., and Yo.Y. measured the electrochemical property of highly dispersed defective $FePO_4$. M.H. and K.Y. performed the charge−discharge test and XAS of olivine-type $FePO_4$. K.O. performed the X-ray scattering analysis. P.R. and P.S. analyzed the electrochemical measure-

ments and XRD data. K.N. supervised the work. All authors contributed to writing the text.

Notes

The authors declare no competing financial interest.

■ ACKNOWLEDGMENTS

This work was financially supported by the Japan Society for the Promotion of Science for Grant-in-Aid for Young Scientists (A) Grant Number 15H05500, Grant-in-Aid for Scientific Research(B) Grant Number 19H02694, and JGC-S Scholarship Foundation. The synchrotron radiation experiments were performed at SPring-8 with the approval of the Japan Synchrotron Radiation Research Institute (JASRI) (Proposal nos. 2015B1809, 2016A1769, 2016B1515, 2016B1522, 2017B1493, 2018A1355, 2018B1429, 2019A1264, and 2019A1274, 2019B1401). The authors are grateful to Dr. McMahon Thomas Homer Reid for helpful discussion and proofreading.

■ REFERENCES

(1) Muldoon, J.; Bucur, C. B.; Gregory, T. Quest for Nonaqueous Multivalent Secondary Batteries: Magnesium and Beyond. *Chem. Rev.* **2014**, *114*, 11683−11720.

(2) Matsui, M. Study on electrochemically deposited Mg metal. *J. Power Sources* **2011**, *196*, 7048−7055.

(3) Besenhard, J. O.; Winter, M. Advances in battery technology: Rechargeable magnesium batteries and novel negative-electrode materials for lithium ion batteries. *ChemPhysChem* **2002**, *3*, 155−159.

(4) Davidson, R.; Verma, A.; Santos, D.; Hao, F.; Fincher, C.; Xiang, S.; Van Buskirk, J.; Xie, K.; Pharr, M.; Mukherjee, P. P.; Banerjee, S. Formation of Magnesium Dendrites during Electrodeposition. *ACS Energy Lett.* **2019**, *4*, 375−376.

(5) Hans Wedepohl, K. The composition of the continental crust. *Geochim. Cosmochim. Acta* **1995**, *59*, 1217−1232.

(6) Yoo, H. D.; Shterenberg, I.; Gofer, Y.; Gershinsky, G.; Pour, N.; Aurbach, D. Mg rechargeable batteries: an on-going challenge. *Energy Environ. Sci.* **2013**, *6*, 2265−2279.

(7) Aurbach, D.; Lu, Z.; Schechter, A.; Gofer, Y.; Gizbar, H.; Turgeman, R.; Cohen, Y.; Moshkovich, M.; Levi, E. Prototype systems for rechargeable magnesium batteries. *Nature* **2000**, *407*, 724−727.

(8) Canepa, P.; Sai Gautam, G.; Hannah, D. C.; Malik, R.; Liu, M.; Gallagher, K. G.; Persson, K. A.; Ceder, G. Odyssey of Multivalent Cathode Materials: Open Questions and Future Challenges. *Chem. Rev.* **2017**, *117*, 4287−4341.

(9) Shannon, R. D. Revised effective ionic radii and systematic studies of interatomic distances in halides and chalcogenides. *Acta Crystallogr., Sect. A: Found. Adv.* **1976**, *32*, 751−767.

(10) Levi, E.; Levi, M. D.; Chasid, O.; Aurbach, D. A review on the problems of the solid state ions diffusion in cathodes for rechargeable Mg batteries. *J. Electroceram.* **2009**, *22*, 13−19.

(11) Rong, Z.; Malik, R.; Canepa, P.; Sai Gautam, G.; Liu, M.; Jain, A.; Persson, K.; Ceder, G. Materials Design Rules for Multivalent Ion Mobility in Intercalation Structures. *Chem. Mater.* **2015**, *27*, 6016−6021.

(12) Sun, X.; Bonnick, P.; Duffort, V.; Liu, M.; Rong, Z.; Persson, K. A.; Ceder, G.; Nazar, L. F. A high capacity thiospinel cathode for Mg batteries. *Energy Environ. Sci.* **2016**, *9*, 2273−2277.

(13) Gu, Y.; Katsura, Y.; Yoshino, T.; Takagi, H.; Taniguchi, K. Rechargeable magnesium-ion battery based on a $TiSe_2$-cathode with d-p orbital hybridized electronic structure. *Sci. Rep.* **2015**, *5*, No. 12486.

(14) Son, S.-B.; Gao, T.; Harvey, S. P.; Steirer, K. X.; Stokes, A.; Norman, A.; Wang, C.; Cresce, A.; Xu, K.; Ban, C. An artificial interphase enables reversible magnesium chemistry in carbonate electrolytes. *Nat. Chem.* **2018**, *10*, 532−539.

(15) Nam, K. W.; Kim, S.; Lee, S.; Salama, M.; Shterenberg, I.; Gofer, Y.; Kim, J.-S.; Yang, E.; Park, C. S.; Kim, J.-S.; Lee, S.-S.; Chang, W.-S.; Doo, S.-G.; Jo, Y. N.; Jung, Y.; Aurbach, D.; Choi, J. W. The High Performance of Crystal Water Containing Manganese Birnessite Cathodes for Magnesium Batteries. *Nano Lett.* **2015**, *15*, 4071−4079.

(16) Gershinsky, G.; Yoo, H. D.; Gofer, Y.; Aurbach, D. Electrochemical and Spectroscopic Analysis of Mg^{2+} Intercalation into Thin Film Electrodes of Layered Oxides: V_2O_5 and MoO_3. *Langmuir* **2013**, *29*, 10964−10972.

(17) Hayashi, M.; Arai, H.; Ohtsuka, H.; Sakurai, Y. Electrochemical Insertion/Extraction of Calcium Ions Using Crystalline Vanadium Oxide. *Electrochem. Solid-State Lett.* **2004**, *7*, A119−A121.

(18) Amatucci, G. G.; Badway, F.; Singhal, A.; Beaudoin, B.; Skandan, G.; Bowmer, T.; Plitz, I.; Pereira, N.; Chapman, T.; Jaworski, R. Investigation of Yttrium and Polyvalent Ion Intercalation into Nanocrystalline Vanadium Oxide. *J. Electrochem. Soc.* **2001**, *148*, A940−A950.

(19) Novák, P.; Imhof, R.; Haas, O. Magnesium insertion electrodes for rechargeable nonaqueous batteries—a competitive alternative to lithium? *Electrochim. Acta* **1999**, *45*, 351−367.

(20) Novák, P.; Desilvestro, J. Electrochemical Insertion of Magnesium in Metal Oxides and Sulfides from Aprotic Electrolytes. *J. Electrochem. Soc.* **1993**, *140*, 140−144.

(21) Parija, A.; Prendergast, D.; Banerjee, S. Evaluation of Multivalent Cation Insertion in Single- and Double-Layered Polymorphs of V_2O_5. *ACS Appl. Mater. Interfaces* **2017**, *9*, 23756−23765.

(22) Verrelli, R.; Black, A. P.; Pattanathummasid, C.; Tchitchekova, D. S.; Ponrouch, A.; Oró-Solé, J.; Frontera, C.; Bardé, F.; Rozier, P.; Palacín, M. R. On the strange case of divalent ions intercalation in V_2O_5. *J. Power Sources* **2018**, *407*, 162−172.

(23) Zhang, R.; Yu, X.; Nam, K.-W.; Ling, C.; Arthur, T. S.; Song, W.; Knapp, A. M.; Ehrlich, S. N.; Yang, X.-Q.; Matsui, M. α-MnO_2 as a cathode material for rechargeable Mg batteries. *Electrochem. Commun.* **2012**, *23*, 110−113.

(24) Kang, B.; Ceder, G. Battery materials for ultrafast charging and discharging. *Nature* **2009**, *458*, 190−193.

(25) Padhi, A. K.; Nanjundaswamy, K. S.; Goodenough, J. B. Phospho-olivines as positive-electrode materials for rechargeable lithium batteries. *J. Electrochem. Soc.* **1997**, *144*, 1188−1194.

(26) Ling, C.; Banerjee, D.; Song, W.; Zhang, M.; Matsui, M. First-principles study of the magnesiation of olivines: redox reaction mechanism, electrochemical and thermodynamic properties. *J. Mater. Chem.* **2012**, *22*, 13517−13523.

(27) Le Poul, N.; Baudrin, E.; Morcrette, M.; Gwizdala, S.; Masquelier, C.; Tarascon, J. M. Development of potentiometric ion sensors based on insertion materials as sensitive element. *Solid State Ionics* **2003**, *159*, 149−158.

(28) Zhang, R.; Ling, C. Unveil the Chemistry of Olivine $FePO_4$ as Magnesium Battery Cathode. *ACS Appl. Mater. Interfaces* **2016**, *8*, 18018−18026.

(29) Naoi, K.; Kurita, T.; Abe, M.; Furuhashi, T.; Abe, Y.; Okazaki, K.; Miyamoto, J.; Iwama, E.; Aoyagi, S.; Naoi, W.; Simon, P. Ultrafast Nanocrystalline-TiO_2(B)/Carbon Nanotube Hyperdispersion Prepared via Combined Ultracentrifugation and Hydrothermal Treatments for Hybrid Supercapacitors. *Adv. Mater.* **2016**, *28*, 6751−6757.

(30) Naoi, K.; Kisu, K.; Iwama, E.; Nakashima, S.; Sakai, Y.; Orikasa, Y.; Leone, P.; Dupre, N.; Brousse, T.; Rozier, P.; Naoi, W.; Simon, P. Ultrafast charge-discharge characteristics of a nanosized core-shell structured $LiFePO_4$ material for hybrid supercapacitor applications. *Energy Environ. Sci.* **2016**, *9*, 2143−2151.

(31) Iwama, E.; Kawabata, N.; Nishio, N.; Kisu, K.; Miyamoto, J.; Naoi, W.; Rozier, P.; Simon, P.; Naoi, K. Enhanced Electrochemical Performance of Ultracentrifugation-Derived nc-Li_3VO_4/MWCNT Composites for Hybrid Supercapacitors. *ACS Nano* **2016**, *10*, 5398−5404.

(32) Naoi, K.; Kisu, K.; Iwama, E.; Sato, Y.; Shinoda, M.; Okita, N.; Naoi, W. Ultrafast Cathode Characteristics of Nanocrystalline-

$Li_3V_2(PO_4)_3$/Carbon Nanofiber Composites. *J. Electrochem. Soc.* **2015**, *162*, A827−A833.
(33) Yonekura, D.; Iwama, E.; Ota, N.; Muramatsu, M.; Saito, M.; Orikasa, Y.; Naoi, W.; Naoi, K. Progress of the conversion reaction of Mn_3O_4 particles as a function of the depth of discharge. *Phys. Chem. Chem. Phys.* **2014**, *16*, 6027−6032.
(34) Naoi, K.; Ishimoto, S.; Miyamoto, J.; Naoi, W. Second generation 'nanohybrid supercapacitor': Evolution of capacitive energy storage devices. *Energy Environ. Sci.* **2012**, *5*, 9363−9373.
(35) Trucano, P.; Chen, R. Structure of graphite by neutron diffraction. *Nature* **1975**, *258*, 136−137.
(36) Zhang, T. B.; Cheng, X. B.; Zhang, Q.; Lu, Y. C.; Luo, G. S. Construction of a cathode using amorphous $FePO_4$ nanoparticles for a high-power/energy-density lithium-ion battery with long-term stability. *J. Power Sources* **2016**, *324*, 52−60.
(37) Fang, Y.; Xiao, L. F.; Qian, J. F.; Ai, X. P.; Yang, H. X.; Cao, Y. L. Mesoporous Amorphous $FePO_4$ Nanospheres as High-Performance Cathode Material for Sodium-Ion Batteries. *Nano Lett.* **2014**, *14*, 3539−3543.
(38) Yin, Y. J.; Wu, P.; Zhang, H.; Cai, C. X. Enhanced cathode performances of amorphous $FePO_4$ hollow nanospheres with tunable shell thickness in lithium ion batteries. *Electrochem. Commun.* **2012**, *18*, 1−3.
(39) Yin, Y.; Hu, Y. J.; Wu, P.; Zhang, H.; Cai, C. X. A graphene-amorphous $FePO_4$ hollow nanosphere hybrid as a cathode material for lithium ion batteries. *Chem. Commun.* **2012**, *48*, 2137−2139.
(40) Larcher, D.; Masquelier, C.; Bonnin, D.; Chabre, Y.; Masson, V.; Leriche, J.-B.; Tarascon, J.-M. Effect of Particle Size on Lithium Intercalation into α-Fe_2O_3. *J. Electrochem. Soc.* **2003**, *150*, A133−A139.
(41) Lu, Z.; Schechter, A.; Moshkovich, M.; Aurbach, D. On the electrochemical behavior of magnesium electrodes in polar aprotic electrolyte solutions. *J. Electroanal. Chem.* **1999**, *466*, 203−217.
(42) Sun, X.; Bonnick, P.; Nazar, L. F. Layered TiS_2 Positive Electrode for Mg Batteries. *ACS Energy Lett.* **2016**, *1*, 297−301.
(43) Mori, T.; Masese, T.; Orikasa, Y.; Huang, Z. D.; Okado, T.; Kim, J.; Uchimoto, Y. Anti-site mixing governs the electrochemical performances of olivine-type $MgMnSiO_4$ cathodes for rechargeable magnesium batteries. *Phys. Chem. Chem. Phys.* **2016**, *18*, 13524−13529.
(44) Orikasa, Y.; Masese, T.; Koyama, Y.; Mori, T.; Hattori, M.; Yamamoto, K.; Okado, T.; Huang, Z. D.; Minato, T.; Tassel, C.; Kim, J.; Kobayashi, Y.; Abe, T.; Kageyama, H.; Uchimoto, Y. High energy density rechargeable magnesium battery using earth-abundant and non-toxic elements. *Sci. Rep.* **2014**, *4*, No. 5622.
(45) Hannah, D. C.; Sai Gautam, G.; Canepa, P.; Ceder, G. On the Balance of Intercalation and Conversion Reactions in Battery Cathodes. *Adv. Energy Mater.* **2018**, *8*, No. 1800379.
(46) Orikasa, Y.; Maeda, T.; Koyama, Y.; Murayama, H.; Fukuda, K.; Tanida, H.; Arai, H.; Matsubara, E.; Uchimoto, Y.; Ogumi, Z. Transient Phase Change in Two Phase Reaction between $LiFePO_4$ and $FePO_4$ under Battery Operation. *Chem. Mater.* **2013**, *25*, 1032−1039.
(47) Thackeray, M. M.; Johnson, P. J.; de Picciotto, L. A.; Bruce, P. G.; Goodenough, J. B. Electrochemical extraction of lithium from $LiMn_2O_4$. *Mater. Res. Bull.* **1984**, *19*, 179−187.
(48) Mizushima, K.; Jones, P. C.; Wiseman, P. J.; Goodenough, J. B. Li_xCoO_2 ($0<x<1$): A new cathode material for batteries of high energy density. *Mater. Res. Bull.* **1980**, *15*, 783−789.
(49) Arthur, T. S.; Kato, K.; Germain, J.; Guo, J.; Glans, P.-A.; Liu, Y.-S.; Holmes, D.; Fan, X.; Mizuno, F. Amorphous V_2O_5−P_2O_5 as high-voltage cathodes for magnesium batteries. *Chem. Commun.* **2015**, *51*, 15657−15660.
(50) Kisu, K.; Iwama, E.; Naoi, W.; Simon, P.; Naoi, K. Electrochemical kinetics of nanostructure $LiFePO_4$/graphitic carbon electrodes. *Electrochem. Commun.* **2016**, *72*, 10−14.

https://dx.doi.org/10.1021/acs.chemmater.9b03665